

# Intrazeolite Anchoring of Co, Ru, and [Ru–Co] Carbonyl Clusters: Synthesis, Characterization, and Their Catalysis for CO Hydrogenation

James G. C. Shen<sup>\*,†</sup> and Masaru Ichikawa<sup>‡</sup>

Lash Miller Chemical Laboratories, Department of Chemistry, University of Toronto, 80 St. George Street, Toronto, Ontario, M5S 3H6 Canada, and Catalysis Research Center, Hokkaido University, Sapporo 060, Japan

Received: September 16, 1997; In Final Form: April 21, 1998

This paper focuses on the intrazeolite anchoring of Co, Ru, and Ru–Co carbonyl clusters and their catalytic performances for CO hydrogenation. The synthesis of intrazeolite anchoring of  $[\text{HRuCo}_3(\text{CO})_9(\mu_2\text{-CO})_3]$  involves the adsorption of metal carbonyl species into zeolite cages followed by reductive carbonylation under a mixed CO and  $\text{H}_2$  atmosphere. The physicochemical characterization used a multianalytical approach, including FT-IR and EXAFS spectroscopies and CO/ $\text{H}_2$  gas chemisorption. The research concluded several key points as follows. (i) There is significant bimetallic interaction. (ii) The generation process of bimetallic carbonyl clusters was considered to occur through the interaction of  $[\text{Ru–Co}]$ ,  $\text{Co}(\text{CO})_4^-$ , and  $\text{Ru}^I$  carbonyls, and conversion into  $[\text{HRuCo}_3(\text{CO})_9(\mu_3\text{-CO})_3]$  and further to  $[\text{HRuCo}_3(\text{CO})_9(\mu_2\text{-CO})_3]$  isomer. (iii) Internal and external confinement of  $[\text{HRuCo}_3(\text{CO})_9(\mu_3\text{-CO})_3]$  were compared. (iv) The intrazeolite anchoring of  $[\text{RuCo}_3]$  carbonyl clusters shows a strong reaction with the extraframework  $\text{Na}^+$   $\alpha$ -cage cations through involvement of the oxygen end of the bridging carbonyl ligands. (v) The bimetallic Ru–Co cluster catalyst shows higher CO conversion and oxygenates selectivity than the monometallic Co or Ru cluster. A high Co ratio in the Ru–Co cluster catalyst enhances the catalytic activity and the selectivity of oxygenates. (vi) The catalytic properties such as oxygenates selectivity depend on cluster size. Basic NaX is superior to NaY in enhancing oxygenates selectivity. (vii) Infrared spectra,  $^{13}\text{CO}$ ,  $\text{D}_2$  isotopic exchange, and mass studies prove that a surface  $\eta^2$ -formyl species adsorbed on Ru–Co interaction sites is an intermediate of oxygenate formation. The adjacent Ru–Co sites suppress  $\eta^2$ -formyl adspecies dissociation and promote formyl species insertion into alkyl adspecies to enhance heavy oxygenate formation. (ix) The deactivated bimetallic Ru–Co cluster catalyst can be regenerated by hydrogen treatment, whereas the monometallic Co cluster catalyst cannot be regenerated.

## 1. Introduction

Loading organometallic and coordination compounds into dehydrated zeolite cages in many cases modifies the chemistry and physical properties of both the “guest” and the “host”. The zeolite structure is responsible for a high internal electric field,<sup>1</sup> for the presence of “coordinatively unsaturated” extraframework cations,<sup>2</sup> and for an oxide framework that may contain Brønsted acid, Lewis acid, and Lewis base sites.<sup>3</sup> The zeolite consequently acts as a “solid solvent”.

In this regard, the zeolite-mediated synthesis of metal carbonyl clusters can provide routes to compounds not accessible through conventional solution techniques, as well as delivering a higher clusters yield. In addition, an investigation of zeolite-mediated synthesis can be expected to provide a better understanding of the nucleation process of cluster formation and of the resulting chemical properties. For example,  $[\text{Co}_4(\text{CO})_{12}]$ <sup>4</sup> and  $[\text{Co}_6(\text{CO})_{16}]$ <sup>5</sup> have been synthesized from  $[\text{Co}_2(\text{CO})_8]$  in zeolite cages;  $[\text{HCoRu}_3(\text{CO})_{13}]$ <sup>6</sup> has been formed from the reaction between  $[\text{Co}(\text{CO})_4]^-$  and  $\text{Ru}^I(\text{CO})_2$  in NaY cages;  $[\text{Ru}_3(\text{CO})_{12}]$  in NaY cages, when thermally activated in a hydrogen atmosphere, has been shown to generate intrazeolitic  $[\text{H}_4\text{Ru}_4(\text{CO})_{12}]$ ;<sup>7</sup> and the intrazeolite anchoring of  $[\text{HRu}_6(\text{CO})_{18}]^-$ <sup>8</sup> and  $[\text{Ru}_6(\text{CO})_{18}]^{2-}$ <sup>9</sup> has been obtained by the reductive carbonyla-

tion of  $\text{Ru}^{3+}$ -exchanged NaY and  $\text{Ru}^{3+}$ -exchanged NaX. The syntheses of these metal carbonyl clusters and their activated decarbonylated catalyst states are listed in Table 1. Their properties have been studied in detail and published.<sup>4–9</sup> None of the investigations hitherto available, however, has effectively addressed the preparation of bimetallic clusters with uniform nuclearities in zeolite cages. When bimetallic carbonyl clusters are decarbonylated, or when, under catalytic reaction conditions, metal is leached from them and transformed to ill-defined microparticles, the structure of the bimetallic cluster is lost.<sup>10</sup> The interaction and the interconversion of molecular metal carbonyls have not been well characterized. In this context, our present research focuses on the design and synthesis of nanoscopic Ru–Co bimetallic carbonyl clusters,  $[\text{HRuCo}_3(\text{CO})_{12}]$ , inside zeolite cages. We use a multianalytical approach, including infrared and EXAFS (extended X-ray absorption fine structure) spectroscopies and CO/ $\text{H}_2$  gas chemisorption, to characterize the structure and properties of such clusters. We study the reversible decarbonylation–recarbonylation of  $[\text{HRuCo}_3(\text{CO})_{12}]$  in zeolite cages, including the combination of  $[\text{Ru–Co}]$  species and of  $\text{Ru}^I$  and Co carbonyls and the conversion of  $\text{RuCo}_3$  carbonyls to structural isomers.

The use of metal carbonyl clusters as catalyst precursors is an important aspect in homogeneous and heterogeneous catalysis.<sup>11–13</sup> The intrazeolitic anchoring of such entities results in metal clusters with a very high metal dispersion and a well-defined metal composition. Such clusters are expected to have

\* To whom correspondence should be addressed. E-mail: gshen@chem.utoronto.ca.

<sup>†</sup> University of Toronto.

<sup>‡</sup> Hokkaido University.

TABLE 1: Preparation and Decarbonylation of the Intrazeolitic Co, Ru, and Ru–Co Carbonyl Clusters

precursor	preparation	decarbonylation	decarbonylated sample <sup>a</sup>
[Co <sub>4</sub> (CO) <sub>12</sub> ]/NaY <sup>4</sup> (10 wt % Co loading)	Dehydrated NaY was mixed mechanically with C <sub>2</sub> (CO) <sub>8</sub> under N <sub>2</sub> followed by 1 h aging at 300 K.	[Co <sub>4</sub> (CO) <sub>12</sub> ]/NaY heated from 300 to 353 K under 200 Torr of O <sub>2</sub> ; kept at 353 K for 1 h	[Co <sub>4</sub> ] <sub>ox</sub> /NaY
		[Co <sub>4</sub> ] <sub>ox</sub> /NaY evacuated at 300 K; heated from 300 to 673 K at 1 K/min under H <sub>2</sub> flow; kept at 673 K for 6 h	[Co <sub>4</sub> ] <sub>red</sub> /NaY
[Co <sub>6</sub> (CO) <sub>16</sub> ]/NaY <sup>5</sup> (10 wt % Co loading)	Adsorption of Co <sub>2</sub> (CO) <sub>8</sub> onto a THF slurry of NaY, heated from 298 to 313 K under 300 Torr of CO and 100 Torr of H <sub>2</sub> .	[Co <sub>6</sub> (CO) <sub>16</sub> ]/NaY heated from 300 to 353 K under 200 Torr of O <sub>2</sub> ; kept at 353 K for 1 h	[Co <sub>6</sub> ] <sub>ox</sub> /NaY
		[Co <sub>6</sub> ] <sub>ox</sub> /NaY evacuated at 300 K; heated from 300 to 673 K at 1 K/min under H <sub>2</sub> flow; kept at 673 K for 6 h	[Co <sub>6</sub> ] <sub>red</sub> /NaY
[Ru <sub>3</sub> (CO) <sub>12</sub> ]/NaY <sup>6</sup> (3.2 wt % Ru loading)	Dehydrated NaY was mixed mechanically with Ru <sub>3</sub> (CO) <sub>12</sub> under N <sub>2</sub> followed by heating at 333 K for 48 h in vacuum.	[Ru <sub>3</sub> (CO) <sub>12</sub> ]/NaY heated from 300 to 623 K at 5 K/min under a mixed gas of 5% H <sub>2</sub> and 95% He; kept at 623 K for 2 h	[Ru <sub>3</sub> ] <sub>red</sub> /NaY
[HRu <sub>6</sub> (CO) <sub>18</sub> ] <sup>−</sup> /NaY <sup>8</sup> (3.2 wt % Ru loading)	[Ru(NH <sub>3</sub> ) <sub>6</sub> ] <sup>3+</sup> /NaY was exposed to 200 Torr of CO and 200 Torr of H <sub>2</sub> followed by heating from 300 to 413 K.	[Ru <sub>6</sub> (CO) <sub>18</sub> ] <sup>−</sup> /NaY heated from 300 to 623 K under a mixed gas of 5% H <sub>2</sub> and 95% He at 5 K/min flow rate; kept at 623 K for 2 h	[Ru <sub>6</sub> ] <sub>red</sub> /NaY
[Ru <sub>6</sub> (CO) <sub>18</sub> ] <sup>2−</sup> /NaX <sup>9</sup> (3.2 wt % Ru loading)	[Ru(NH <sub>3</sub> ) <sub>6</sub> ] <sup>3+</sup> /NaX was exposed to 200 Torr of CO and 200 Torr of H <sub>2</sub> followed by heating from 300 to 393 K.	[Ru <sub>6</sub> (CO) <sub>18</sub> ] <sup>2−</sup> /NaX heated from 300 to 623 K at 5 K/min under a mixed gas of 5% H <sub>2</sub> and 95% He; kept at 623 K for 2 h	[Ru <sub>6</sub> ] <sub>red</sub> /NaX
[HRu <sub>3</sub> Co(CO) <sub>13</sub> ]/NaY <sup>6</sup> (3.2 wt % Ru loading; 0.6 wt %, Co loading)	[Ru <sub>3</sub> (CO) <sub>12</sub> ]/NaY immersed in THF of Co <sub>2</sub> (CO) <sub>8</sub> ; removed THF; heated from 300 to 413 K.	[HRu <sub>3</sub> Co(CO) <sub>13</sub> ]/NaY heated from 300 to 573 K at 1 K/min under 400 Torr of H <sub>2</sub> ; kept at 573 K for 2 h	[Ru <sub>3</sub> Co] <sub>red</sub> /NaY
[HRuCo <sub>3</sub> (CO) <sub>12</sub> ]/NaY <sup>b</sup> (3.2 wt % Ru loading; 5.6 wt %, Co loading)	[HRu <sub>6</sub> (CO) <sub>18</sub> ] <sup>−</sup> /NaY was exposed to 400 Torr of O <sub>2</sub> , heated from 300 to 473 K, and then kept at 473 K for 2 h to give [Ru <sub>x</sub> ] <sub>ox</sub> /NaY. [Ru <sub>x</sub> ] <sub>ox</sub> /NaY immersed in THF of Co <sub>2</sub> (CO) <sub>8</sub> ; removed THF; heated from 300 to 353 K.	[HRuCo <sub>3</sub> (CO) <sub>12</sub> ]/NaY heated from 300 to 523 K at 1 K/min under 450 Torr of H <sub>2</sub> ; kept at 523 K for 2 h	[RuCo <sub>3</sub> ] <sub>red</sub> /NaY

<sup>a</sup> Subscripts 3, 4, and 6 of decarbonylated samples only signify them as resulting from precursors having 3, 4, and 6, subscripts. <sup>b</sup> This work.

catalytic properties superior to those of a conventionally prepared metal catalyst. In addition, the oxide framework of the zeolite is considered to be a macrospheroidal, multisite, and multidentate “zeolate” ligand.<sup>14</sup> The combination with metallic clusters is expected to carry great potential for favoring activation and selective catalysis in CO hydrogenation.

The addition of metal ions, such as Mn, Ti, Zr, Nb, and Fe, promotes the production of oxygenates, including alcohols and aldehydes, in CO hydrogenation on the modified Rh, Ir, and Pd catalysts.<sup>15,16</sup> EXAFS,<sup>15</sup> Mössbauer,<sup>16</sup> XPS,<sup>17</sup> and FT-IR<sup>18</sup> studies of such bimetallic catalysts suggest that the promotion is associated with CO activation on surface bimetallic sites of the catalyst and that this promotion enhances the migratory CO insertion into several intermediate adspecies such as methyl and carbene.<sup>19</sup> The intrazeolitic bimetallic clusters are unique, bringing nanostructural alloys with encasing on a nearly molecular scale. These clusters consequently offer the prospect of synergetic effects in CO hydrogenation, differing strongly from the effects achievable with individual metallic cluster components. Thus, research on CO hydrogenation over these alloy clusters is expected to reveal relevant details such as reactive intermediates, reaction steps, overall catalytic reaction mechanism, and relations among reaction rate, clusters structure, and host zeolite potential.

This paper reports on CO hydrogenation on intrazeolitic Co, Ru, and [Ru–Co] clusters. The catalytic activity and selectivity for the production of oxygenates, the reaction intermediate, and the reaction mechanism are demonstrated and discussed on the basis of reaction kinetics, infrared spectroscopy, isotopic reaction, and mass number studies. Furthermore, the

deactivation and the regeneration of the cluster catalysts are explored.

## 2. Results and Discussion

### 2.1. Comprehensive Structural and Spectroscopic Study of Intrazeolite Anchoring of [Ru–Co] Carbonyl Clusters.

**2.1.1. Infrared Characterization for the Interaction of [Ru<sub>x</sub>]<sub>ox</sub> and Co<sub>2</sub>(CO)<sub>8</sub> Clusters with CO and H<sub>2</sub> in NaY Zeolite.** Figure 1C shows in situ infrared spectra of the reaction of [Ru<sub>x</sub>]<sub>ox</sub>/NaY + Co<sub>2</sub>(CO)<sub>8</sub> with 300 Torr of CO + 150 Torr of H<sub>2</sub> at 353 K. The terminal CO bands and the bridging CO band appear, respectively, at (2084, 2064, 2036, and 1989 cm<sup>−1</sup>) and 1798 cm<sup>−1</sup>, denoted as sample A (Figure 1C, line a and Table 2). After 0.5–16 h of heating at 353 K, the terminal bands at 2084, 2064, 2036, and 1989 cm<sup>−1</sup> remained at constant frequency, whereas the bridging band shifted from a broad band at 1798 cm<sup>−1</sup> to a narrow band at 1812 cm<sup>−1</sup> during the growth of the peak intensity (Figure 1C, lines a–j). The resulting deep brown sample is denoted as sample B. The spectrum [ $\nu_{\text{cot}}$ , 2084 (vs), 2064 (vs), 2036 (s), 1989 (m);  $\nu_{\text{cob}}$ , 1812 (s) cm<sup>−1</sup>] (Figure 1C, line j, and Table 2) closely resembled the spectrum of [HRuCo<sub>3</sub>(CO)<sub>9</sub>( $\mu_2$ -CO)<sub>3</sub>] in a tetrahydrofuran (THF) solution [ $\nu_{\text{cot}}$ , 2070 (vs), 2062 (vs), 2030 (s), 1985 (m);  $\nu_{\text{cob}}$ , 1884 (m) cm<sup>−1</sup>], which has three edge-bridging CO and nine terminal CO ligands.<sup>20</sup> [HRuCo<sub>3</sub>(CO)<sub>9</sub>( $\mu_2$ -CO)<sub>3</sub>] appears to be formed in NaY zeolite. It should be noted that the stretching frequency of the bridging carbonyl band  $\nu_{\text{cob}}$  is red-shifted by about 72 cm<sup>−1</sup>, while the terminal carbonyl bands  $\nu_{\text{cot}}$  are blue-shifted by about 4–14 cm<sup>−1</sup> with respect to those of crystalline

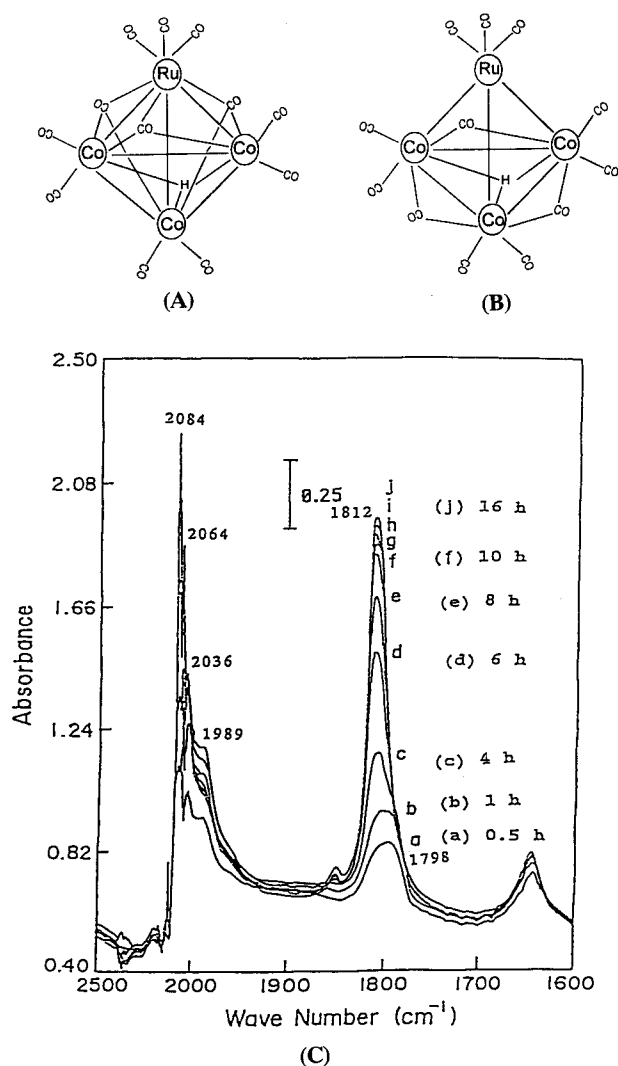


**Figure 1.** (A) Molecular configuration of  $[\text{HRuCo}_3(\text{CO})_9(\mu_3\text{-CO})_3]$ . (B) Molecular configuration of  $[\text{HRuCo}_3(\text{CO})_9(\mu_2\text{-CO})_3]$ . (C) In situ infrared spectra of the reductive carbonylation of  $[\text{Ru}]_{\text{ox}}/\text{Na}_{56}\text{Y}$  and  $\text{Co}_2(\text{CO})_8$  by 300 Torr of CO with 150 Torr of  $\text{H}_2$  during heating at 298–353 K: (a) 353 K, 30 min.; (b) 353 K, 1 h; (c) 353 K, 4 h; (d) 353 K, 6 h; (e) 353 K, 8 h; (f) 353 K, 10 h; (g) 353 K, 12 h; (h) 353 K, 13 h; (i) 353 K, 14 h; (j) 353 K, 16 h.

$[\text{HRuCo}_3(\text{CO})_9(\mu_2\text{-CO})_3]$ .<sup>20</sup> This red shift is consistent with the formation of ion pairs including the oxygen end of carbonyl ligands and extraframework  $\text{Na}^+$  cations of zeolite cages.<sup>4–6</sup>

**2.1.2. EXAFS Data Characterization for the Intrazeolite Anchoring of Ru–Co Carbonyl Clusters.** To obtain more insight into the structure of Ru–Co carbonyl clusters, especially into the metal framework, the EXAFS spectra of the Co K-edge and the Ru K-edge were analyzed through a fitting of the curves to a plane-wave multiple-scattering formula.<sup>21</sup> The EXAFS function was obtained from the average of X-ray absorption spectra by a cubic spline background subtraction and was then normalized through division by the height of the absorption edge. Empirical phase-shift and amplitude functions were extracted for this analysis from the crystalline  $[(\text{PH}_3\text{P})_2\text{Nj}][\text{RuCo}_3(\text{CO})_{12}]$  for the Ru–C, Co–C, Ru–Co, Co–Co, Ru(–C–)O, and Co(–C–)O bonds. The raw EXAFS data characterizing sample B at the Ru K-edge (Figure 2Ai) show oscillations up to a value of  $K$ , the wave vector, of about  $13.5 \text{ \AA}^{-1}$ , clearly indicating the presence of near-neighbor backscatters of high atomic weight. These scatterers are inferred to be Co atoms. The Fourier transform (Figure 2Aii) was obtained

from the raw EXAFS data with a  $K^3$ -weighting in the range  $3.0 < K < 14.0 \text{ \AA}^{-1}$ . The Fourier transformed data were then inverse-transformed in the  $1.82 \text{ \AA} < R < 2.67 \text{ \AA}$  region (where  $R$  is the distance from the absorber Ru atom) to isolate both the major contributions from low-frequency noise and the higher-shell contributions. Since the infrared data indicate that carbonyl ligands were also present in sample B, the peak in the range  $1.82 \text{ \AA} < R < 2.67 \text{ \AA}$  is attributable to three-shell contributions of Ru–Co, Ru–C, and Ru(–C–)O. Since the Ru(–C–)O contribution was found to be strongly coupled with the Ru–Co contribution, it is necessary to analyze these two contributions simultaneously. The structural parameters were estimated initially by fitting the data in the high- $K$  range ( $8.5 \text{ \AA} < K < 15 \text{ \AA}$ ). The multiple scattering associated with Ru(–C–)O groups was found to be significant, whereas the Ru–C contribution was found to be negligible in this range. Further analysis, following the subtraction of the calculated Ru–Co and Ru(–C–)O contributions from the raw data, led to characterization of the Ru–C contribution. The initial guesses for parameter estimation were obtained by a satisfactory fit of the raw data with the sum of the three contributions. The Ru–Co, Ru(–C–)O, and Ru–C contributions were then analyzed simultaneously through the adjustment of the parameters of the initial estimates. The iteration was continued until good overall agreement was obtained. The results of the curve-fitting analyses with the best calculated coordination parameters are shown in Figure 2Aiii and Table 3. This procedure yielded the following results for sample B: Ru–Co coordination numbers of 2.80 at an average distance of  $2.62 \text{ \AA}$ ; Ru–C coordination numbers of 2.87 at an average distance of  $1.90 \text{ \AA}$ ; and Ru(–C–)O coordination numbers of 2.79 at an average distance of  $3.03 \text{ \AA}$ .

The raw EXAFS data, the  $K^3$ -weighted phase- and amplitude-corrected Fourier transform, and the curve-fitting of sample B at the Co K-edge are shown in parts Bi, Bii, and Biii of Figure 2. The statistical analytical method for a four-shell contribution of Co–Co, Co–Ru, Co–C, and Co(–C–)O at the Co K-edge is similar to that presented above for the Ru K-edge. All the Co atoms in sample B are stereochemically equivalent, with each bonded to 0.80 Ru atoms at an average Co–Ru bond length of  $2.62 \text{ \AA}$ , to 1.90 Co atoms at an average Co–Co bond length of  $2.52 \text{ \AA}$ , to 2.84 C ligands at an average Co–C bond length of  $1.80 \text{ \AA}$ , and to 2.80 O ligands at an average Co(–C–)O bond length of  $3.05 \text{ \AA}$  (Table 4).

Tables 3 and 4 present the results of the curve-fitting analysis with best calculated coordination parameters for sample A. In terms of EXAFS data analysis, the Co K-edge observation of Co–Co ( $R = 2.52 \text{ \AA}$ ,  $N = 1.90$ ) and Co–Ru ( $R = 2.63 \text{ \AA}$ ,  $N = 0.81$ ) and the Ru K-edge observation of Ru–Co ( $R = 2.62 \text{ \AA}$ ,  $N = 2.79$ ) are essentially equivalent to the corresponding observation obtained for sample B. This implies that the samples have the same framework. The number of CO ligands around Co increases from 2.34 in sample A to 2.84 in sample B, and the number of CO ligands around Ru decreases from 3.62 in sample A to 2.87 in sample B. The average distance of Co–C ( $1.80 \text{ \AA}$  in sample A,  $1.81 \text{ \AA}$  in sample B), Co(–C–)O ( $3.05 \text{ \AA}$ ,  $3.06 \text{ \AA}$ ), Ru–C ( $1.90 \text{ \AA}$ ,  $2.02 \text{ \AA}$ ), and Ru(–C–)O ( $3.03 \text{ \AA}$ ,  $3.06 \text{ \AA}$ ) are practically identical for the two samples (Tables 3 and 4). These results for the number of ligands and average distances suggest that samples A and B are structural isomers with a tetrahedral  $\text{RuCo}_3$  cluster framework. The reductive carbonylation from sample A to sample B in a mixed CO and  $\text{H}_2$  atmosphere results in a variety of M–CO contributions but has no effect on M–M contributions.

**TABLE 2: Assignment of the Carbonyl Species on the Sample of CO<sub>ad</sub>-Ru/Co<sub>3</sub>/NaY**

	sample A	sample B	Ru intermediate	Co intermediate	recarbonylated sample
$\nu_{\text{CO}}$	2084 vs, 2064 vs, 2036 s, 1898 m	2084 vs, 2064 vs, 2036 s, 1812 s	2086, 2026	1950, 1907	2084 vs, 2064 vs, 2040 s, 1814 s
$A_t/A_f$ or $e^a$	1.32	1.15			1.12
abundance	0.72 <sup>b</sup>	1 <sup>b</sup>	0.30 <sup>c</sup>	0.24 <sup>c</sup>	0.89 <sup>b</sup>
assignment	[HRuCo <sub>3</sub> (CO) <sub>9</sub> ( $\mu_3$ -CO) <sub>3</sub> ]/NaY	[HRuCo <sub>3</sub> (CO) <sub>9</sub> ( $\mu_2$ -CO) <sub>3</sub> ]/NaY	Ru <sup>I</sup> (CO) <sub>2</sub> /NaY	Co(CO) <sub>4</sub> <sup>-</sup> /NaY	[HRuCo <sub>3</sub> (CO) <sub>9</sub> ( $\mu_2$ -CO) <sub>3</sub> ]/NaY

<sup>a</sup>  $A_t$ ,  $A_f$ , and  $A_e$  are the integrated areas of the IR bands for CO<sub>t</sub>, CO<sub>f</sub>, and CO<sub>e</sub>, respectively. t, terminal CO bands; f, face-bridging bands; e, edge-bridging CO bands. <sup>b</sup> Based on the ratio of the integrated areas of  $\nu_{\text{CO}}$  for synthesis chemical species and sample B. <sup>c</sup> Based on the ratio of the integrated areas of  $\nu_{\text{CO}}$  for synthesis chemical species and recarbonylated sample.

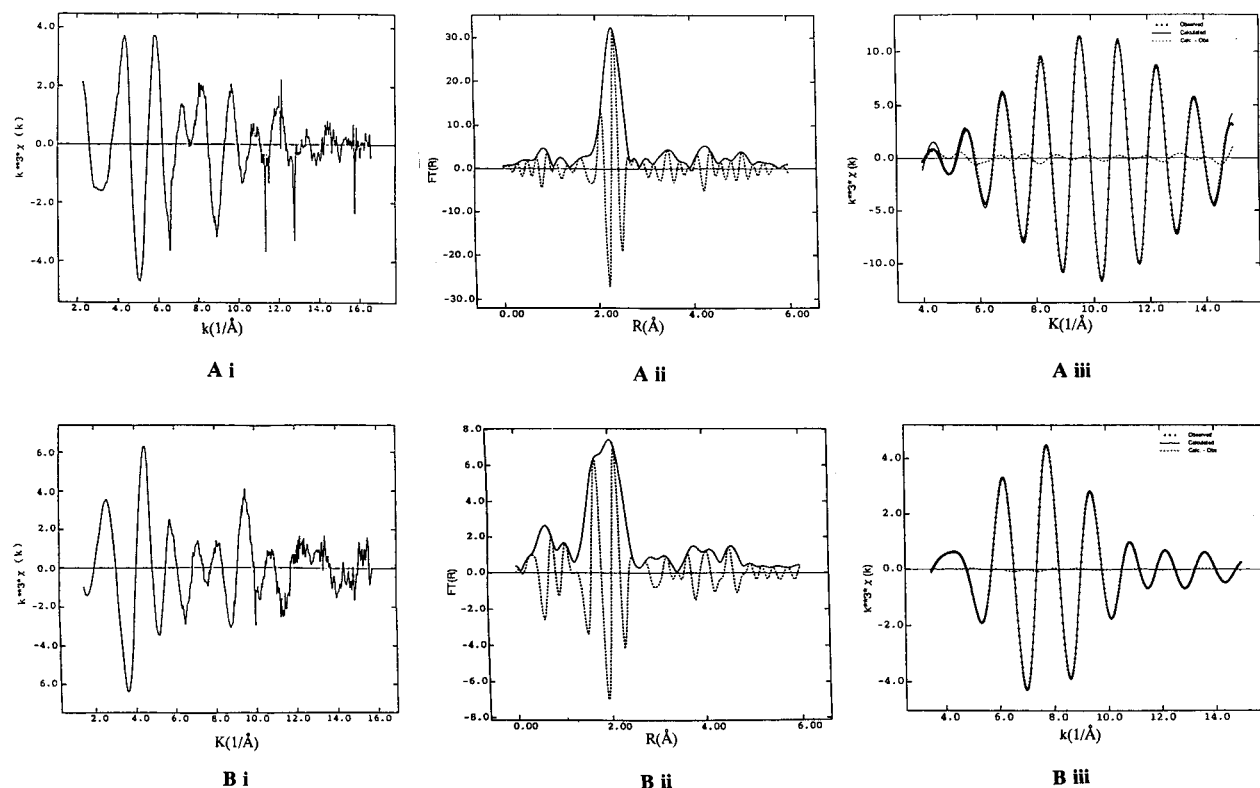


**Figure 2.** Results of EXAFS with the best calculated coordination parameters characterizing sample B: (Ai) raw EXAFS data at the Ru K-edge; (Aii) Ru K-edge data, Fourier transform of  $k^3$ -weighted EXAFS spectrum  $k^3\chi(k)$  vs  $R$ ; (Aiii) Ru K-edge data, inverse Fourier transform of experimental EXAFS in the range  $1.82 \text{ \AA} < R < 2.67 \text{ \AA}$  (dashed curve) and sum of the calculated Ru-Co + Ru-C + Ru(-C)-O contribution (solid curve); (Bi) raw EXAFS data at the Co K-edge; (Bii) Co K-edge data, Fourier transform of  $k^3$ -weighted EXAFS spectrum  $k^3\chi(k)$  vs  $R$ ; (Biii) Co K-edge data, inverse Fourier transform of experimental EXAFS in the range  $1.25 \text{ \AA} < R < 2.55 \text{ \AA}$  (dashed curve) and sum of the calculated Co-Co + Co-Ru + Co-C + Co(-C)-O contribution (solid curve).

**TABLE 3: EXAFS Results Characterizing the Zeolite-Supported Ru-Co Carbonyl Species at Ru K-Edge<sup>a</sup>**

sample	Ru K-edge											
	Ru-Co				Ru-C				Ru(-C)-O			
	$N$	$R/\text{\AA}$	$\Delta E_0/\text{eV}$	$\sigma/\text{\AA}$	$N$	$R/\text{\AA}$	$\Delta E_0/\text{eV}$	$\sigma/\text{\AA}$	$N$	$R/\text{\AA}$	$\Delta E_0/\text{eV}$	$\sigma/\text{\AA}$
sample B	2.80	2.62	9.84	0.041	2.87	1.90	-0.71	0.033	2.79	3.03	-5.36	0.052
sample A	2.79	2.62	-3.24	0.072	3.62	2.02	5.32	0.068	3.74	3.06	8.72	0.038
decarbonylated sample	1.10	2.63	7.23	0.058								
recarbonylated sample	2.77	2.63	-11.25	0.037	2.90	1.90	8.32	0.054	3.01	3.02	7.46	0.025
XRD <sup>b</sup>	3.00	2.63			3.00	1.91			3.00	3.03		

<sup>a</sup> Note:  $N$ , coordination number for absorber-backscatterer pair;  $R$ , radial absorber-backscatterer distance;  $\sigma$ , Debye-Waller factor;  $\Delta E_0$ , inner potential correction. <sup>b</sup> XRD analysis for  $[(\text{Ph}_3\text{P})_2\text{N}][\text{RuCo}_3(\text{CO})_{12}]$ .

The EXAFS results provide strong evidence that the backscatters in the immediate vicinity of the Co absorber atoms of the two samples include Ru and Co. The data measured near the Ru edge further confirm the Ru-Co interaction. The low atomic weight and multiple backscatters were determined as CO groups. In agreement with EXAFS data, the infrared principal  $\nu_{\text{CO}}$  bands for sample B at 2084 and 2064  $\text{cm}^{-1}$  are assigned to the symmetric and antisymmetric stretching of the

two CO ligands bound to each Co atom in  $[\text{HRuCo}_3(\text{CO})_9(\mu_2\text{-CO})_3]$ ; the 2080, 2064, and 2036  $\text{cm}^{-1}$  bands are assigned to the CO stretching of the three CO ligands bound to the Ru atom of  $[\text{HRuCo}_3(\text{CO})_9(\mu_2\text{-CO})_3]$ . The 1812  $\text{cm}^{-1}$  band corresponds to the stretching of the three edge-bridging CO ligands each bound to two Co atoms (Figure 1B).

The terminal CO bands of sample A remained constant, but the bridging CO band shifted from 1798  $\text{cm}^{-1}$  (sample A) to



TABLE 4: EXAFS Results Characterizing the Zeolite-Supported Ru–Co Carbonyl Species at Co K-Edge<sup>a</sup>

sample	Co K-edge											
	Co–Co				Co–Ru				Co–C			
	<i>N</i>	<i>R</i> /Å	$\Delta E_0$ /eV	$\sigma^2$ /Å	<i>N</i>	<i>R</i> /Å	$\Delta E_0$ /eV	$\sigma^2$ /Å	<i>N</i>	<i>R</i> /Å	$\Delta E_0$ /eV	$\sigma^2$ /Å
sample B	1.90	2.52	4.16	0.057	0.80	2.62	−3.79	0.064	2.84	1.80	−7.71	0.041
sample A	1.90	2.52	7.14	0.063	0.81	2.63	−4.18	0.053	2.34	1.81	−5.23	0.035
decarbonylated sample	0.45	2.53	−3.12	0.043	0.90	2.62	2.89	0.074				
recarbonylated sample	1.86	2.54	5.09	0.073	0.80	2.62	1.97	0.038	2.83	1.78	−6.73	0.052
XRD <sup>b</sup>	2.00	2.52			1.0	2.63			3.00	1.82		3.00

<sup>a</sup> Note: *N*, coordination number for absorber–backscatterer pair; *R*, radial absorber–backscatterer distance;  $\sigma^2$ , Debye–Waller factor;  $\Delta E_0$ , inner potential correction. <sup>b</sup> XRD analysis for [(Ph<sub>3</sub>P)<sub>2</sub>N][RuCo<sub>3</sub>(CO)<sub>12</sub>].

1812 cm<sup>−1</sup> (sample B) with increasing reaction time. Lamb et al.<sup>22</sup> claimed that the basicity of the oxygen in CO ligands of metal carbonyl clusters depends on the CO coordination geometry. Triply bridging CO ligands are more basic than doubly bridging CO ligands, which are significantly more basic than terminal CO ligands. This pattern is borne out in the present apparent shift of bridging CO bands between samples A and B. EXAFS data and the infrared band shift suggest that the 1798 cm<sup>−1</sup> band in sample A ([HRuCo<sub>3</sub>(CO)<sub>9</sub>( $\mu_3$ -CO)<sub>3</sub>]) corresponds to the stretching of three face-bridging CO ligands each bound to two Co atoms and one Ru atom (Figure 1A). We conclude that CO ligands in sample A release their face-bridging ligands, bind to Co–Co, and is thermally converted to its isomer [HRuCo<sub>3</sub>(CO)<sub>9</sub>( $\mu_2$ -CO)<sub>3</sub>] (sample B, Figure 1B). A similar conversion of structural isomers is also observed for Rh<sub>6</sub>(CO)<sub>16</sub>.<sup>23</sup> However, in their compound, edge-bridging CO ligands of octahedral Rh are thermally converted to face-bridging CO ligands of octahedral Rh<sub>6</sub>.<sup>23</sup>

Watters et al.<sup>24a</sup> and Hanson et al.<sup>24b</sup> showed that the adsorption of Co<sub>2</sub>(CO)<sub>8</sub> onto NaY from pentane solution yielded mobile Co(CO)<sub>4</sub><sup>−</sup> and Co<sub>4</sub>(CO)<sub>12</sub> species. They claimed partial reversible decarbonylation of Co<sub>2</sub>(CO)<sub>8</sub> to generate Co(CO)<sub>4</sub><sup>−</sup> in the NaY cages. In the present experiment, Co(CO)<sub>4</sub><sup>−</sup> formed from such a decomposition is small enough to diffuse rapidly through both the supercages left empty after [Ru<sub>x</sub>]<sub>ox</sub> deposition and those partially filled by the [Ru<sub>x</sub>]<sub>ox</sub> cluster. The charged environment, resulting from the large number of Na<sup>+</sup> cations, stabilizes the Co(CO)<sub>4</sub><sup>−</sup> within the supercages, allowing reaction with the [Ru<sub>x</sub>]<sub>ox</sub> under a mixed CO and H<sub>2</sub> atmosphere with heating. The predominant [HRuCo<sub>3</sub>(CO)<sub>9</sub>( $\mu_2$ -CO)<sub>3</sub>]/NaY was synthesized.

**2.1.3. Process of Decarbonylation and Recarbonylation of [HRuCo<sub>3</sub>(CO)<sub>9</sub>( $\mu_2$ -CO)<sub>3</sub>]/NaY.** The [HRuCo<sub>3</sub>(CO)<sub>9</sub>( $\mu_2$ -CO)<sub>3</sub>]/NaY sample was treated with 450 Torr of H<sub>2</sub> at a heating rate of 1 K/min from 298 to 373 K. The 2084 (vs), 2064 (vs), 2036 (s), 1989 (m), and 1812 (s) cm<sup>−1</sup> carbonyl bands remain at constant frequency but with decreasing peak intensity, which is consistent with the uniform nature of the [HRuCo<sub>3</sub>(CO)<sub>9</sub>( $\mu_2$ -CO)<sub>3</sub>]/NaY species. When the sample is heated at 523 K for 2 h, the carbonyl bands completely disappeared to give decarbonylated bimetallic intrazeolite clusters, [Ru/Co]<sub>red</sub>/NaY, as shown in Figure 3, line a.

To investigate the structural variation of the clusters resulting from decarbonylation, the reduced state of sample B, [Ru/Co]<sub>red</sub>/NaY, was characterized by EXAFS spectroscopy. The EXAFS data show some break of a direct Ru–Co interaction and the formation of a new species at the Co K-edge at a distance of 2.62 Å with coordination numbers *N*(Co–Ru) of 0.90 and at a distance of 2.53 Å with coordination numbers *N*(Co–Co) of 0.45. The new species at the Ru K-edge shows a distance of 2.63 Å with coordination numbers *N*(Ru–Co) of 1.10 (Tables 3 and 4). The decarbonylated bimetallic clusters show a

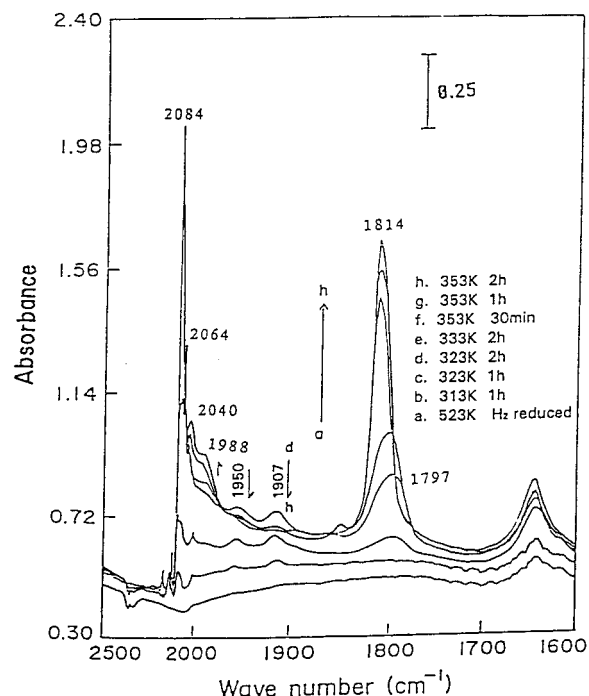


**Figure 3.** In situ infrared spectra characterizing the recarbonylation of the decarbonylated sample B in the presence of 300 Torr of CO and 150 Torr of H<sub>2</sub>: (a) the decarbonylated sample B; (b) 313 K, 1 h.; (c) 323 K, 1 h.; (d) 323 K, 3 h; (e) 333 K, 2 h; (f) 353 K, 30 min.; (g) 353 K, 1 h; (h) 353 K, 2 h.

practically identical distance of Ru–Co, as observed in sample A or B. *N*(Co–Ru) at the Co K-edge remains in the range 0.80–0.90 between sample B and the decarbonylated species, whereas *N*(Co–Ru) at the Ru K-edge decreases to 1.10 for decarbonylated species from 2.79 for sample A or from 2.80 for sample B. The decarbonylated bimetallic species can be detected as [Ru/Co]<sub>red</sub>/NaY on the basis of the ratio of *N*(Ru–Co) around the Ru absorber atom and *N*(Co–Ru) around the Co absorber atom. The coordination numbers of the decarbonylated bimetallic species are much smaller than that of the Co or Ru foil, and even smaller than that of sample A or B. This suggests that the decarbonylated sample maintains the small and highly dispersed particle of the bimetal in the NaY cavities. The zeolite channels, with their limited size, probably prevent metallic particles in the NaY cavities from coalescing.

This decarbonylated sample was recarbonylated by treatment with a mixture of 300 Torr of CO and 150 Torr of H<sub>2</sub> in an infrared cell at 300–353 K. Upon exposure of the gas mixture at 300 K, infrared terminal CO bands appear at 2080 and 2026 cm<sup>−1</sup>, which are ascribed to mononuclear Ru carbonyls, such as Ru(CO)<sub>2</sub>,<sup>6,8,25</sup> bands also appear at 1950 and 1907 cm<sup>−1</sup>, which are ascribed to Co(CO)<sub>4</sub><sup>−</sup> species<sup>6,25</sup> (Figure 3, line b and Table 2). The two infrared bands at 1950 and 1907 cm<sup>−1</sup>

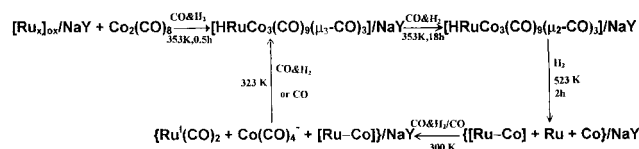


**Figure 4.** Scheme for the chemistry of bimetallic Ru–Co clusters in the NaY cages.

decreased in intensity, whereas the five infrared bands at 2084, 2064, 2040, 1988, and 1797  $\text{cm}^{-1}$  grow in intensity with increasing reaction time and temperature (Figure 3, lines c–e). By comparison of the wavenumbers between Figure 3, line e, and Figure 1C, line a, these five bands are inferred to be an indication of an  $[\text{HRuCo}_3(\text{CO})_9(\mu_3\text{-CO})_3]$  species re-formed inside NaY cages. When the sample was heated to 353 K (Figure 3, line f), the 2084, 2064, 2040, and 1988  $\text{cm}^{-1}$  terminal CO bands remained at constant frequency, but the bridging CO band shifted from 1797 to 1814  $\text{cm}^{-1}$ . The infrared spectrum of the resulting sample (Figure 3, line h) is practically identical with that of  $[\text{HRuCo}_3(\text{CO})_9(\mu_2\text{-CO})_3]/\text{NaY}$  (Figure 1C, line j), as seen from a comparison of the wavenumber values, intensity, and full width at half-maximum (fwhm) of CO bands, as well as the constant area ratio of  $\text{CO}_t$  to  $\text{CO}_b$  bands of  $[\text{HRuCo}_3(\text{CO})_9(\mu_2\text{-CO})_3]/\text{NaY}$  precursors and the recarbonylated sample (Table 2). The EXAFS data of the recarbonylated sample show that the coordination parameters around the Co and Ru absorber atom closely resemble those of sample B (Tables 3 and 4), indicating that  $[\text{HRuCo}_3(\text{CO})_9(\mu_2\text{-CO})_3]$  is re-formed inside NaY cages. The recarbonylated sample became deep-brown again. Here, the  $\nu_{\text{CO}}$  infrared frequencies [2080, 2026, 1950, 1907, and 1797  $\text{cm}^{-1}$ ] and the integrated area of the peaks for the initial sample, as a result of recarbonylation of the decarbonylated sample, are different from those of  $[\text{HRuCo}_3(\text{CO})_9(\mu_2\text{-CO})_3]/\text{NaY}$  (Table 2). This is indicative that  $\text{Ru}^1$  carbonyls,  $\text{Co}(\text{CO})_4^-$ , and  $[\text{HRuCo}_3(\text{CO})_9(\mu_3\text{-CO})_3]$  are intermediates in the regeneration of  $[\text{HRuCo}_3(\text{CO})_9(\mu_2\text{-CO})_3]/\text{NaY}$ . The results are also consistent with the hypothesis that Ru acts as an anchor that inhibits Co agglomeration and stabilizes the bimetallic cluster. A schematic illustration of the proposed mechanism is shown in Figure 4.

The carbonylation–decarbonylation process is reversible under these conditions. Indeed, the process was carried out several times without any significant change in the infrared spectra and EXAFS data of the carbonylated form. However, when much more severe conditions were used for the decarbonylation, e.g.,  $[\text{HRuCo}_3(\text{CO})_9(\mu_2\text{-CO})_3]/\text{NaY}$  was decarbonylated at 673 K, the sample turned dark-gray and could not be recarbonylated as before to give the infrared spectrum and EXAFS data matching those of  $[\text{HRuCo}_3(\text{CO})_9(\mu_2\text{-CO})_3]/\text{NaY}$ . In addition, the successful synthesis of  $[\text{HRuCo}_3(\text{CO})_9(\mu_2\text{-CO})_3]$  also depends on the Co/Ru ratio of the precursors, which is preferably between 2.7 and 3.2. Outside this range, despite the same synthesis condition, the resulting sample is typically gray and the corresponding infrared spectrum shows a terminal CO band at 2045  $\text{cm}^{-1}$  but no bridging CO band. This single peak is indicative of CO adsorbed on metallic Ru particle, similar to those of CO adsorbed on a reduced Ru/ $\text{SiO}_2$  catalyst.<sup>26</sup>

The framework structures of some commonly studied NaY and NaX zeolites are presented in Figure 5a.<sup>27</sup> These microporous aluminosilicates are composed of  $\text{SiO}_4$  and  $\text{AlO}_4^-$  tetrahedra joined through shared oxygen bridges. The large cavity in these zeolites is typically referred to as the  $\alpha$ -cage, while the small cavities are known as the  $\beta$ -cages and the hexagonal prisms. The net negative charge on the lattice is counterbalanced by exchangeable metal Na cations located at

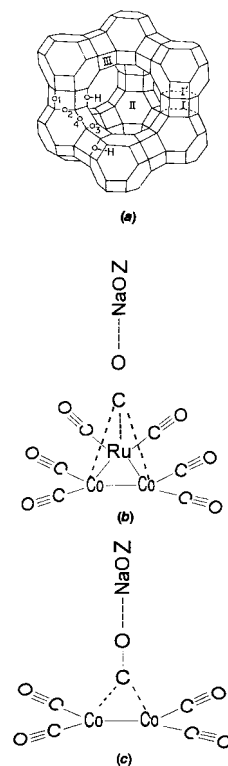


**Figure 5.** (a) Illustration of part of the unit cell of faujasite zeolites, where extraframework cations I, I', II, and III are indicated; (b) possible anchoring site of face-bridging CO ligands bound to two Co atoms and one Ru atom for the  $\alpha$ -cage located in the  $[\text{HRuCo}_3(\text{CO})_9(\mu_3\text{-CO})_3]$  cluster; (c) possible anchoring site of edge-bridging CO ligands bound to two Co atoms for the  $\alpha$ -cage located in the  $[\text{HRuCo}_3(\text{CO})_9(\mu_2\text{-CO})_3]$  cluster.

well-defined sites that are labeled in Figure 5a. Protons act as the charge-balancing cations and are usually incorporated into the framework oxygen by either zeolite preparation or ion exchange in an acid medium, forming hydroxyl groups (Brønsted acidity). These can be directly monitored by the corresponding infrared stretching frequency at 3660  $\text{cm}^{-1}$  occurring inside the zeolite  $\alpha$ -cage (bridging hydroxyls in Figure 5a) and at 3556  $\text{cm}^{-1}$  occurring at small cavities of zeolite.

In another series of experiments, the  $[\text{HRuCo}_3(\text{CO})_9(\mu_2\text{-CO})_3]$  was decarbonylated as before and recarbonylated only in the presence of CO with the same temperature-programmed heating. The infrared bands and EXAFS data showed that  $[\text{HRuCo}_3(\text{CO})_8(\mu_2\text{-CO})_4]/\text{NaY}$  is also re-formed. The results are therefore consistent with the possibility that the bridging hydroxyl inside the NaY cage is the H source of  $[\text{HRuCo}_3(\text{CO})_9(\mu_2\text{-CO})_3]$  and facilitate the synthesis of  $[\text{HRuCo}_3(\text{CO})_9(\mu_2\text{-CO})_3]$  inside NaY cages. EXAFS data identified the decarbonylated bimetallic species as  $[\text{Ru-Co}]$ , and the infrared spectrum confirmed that some isolated Ru and Co are also present. Thus, the regenerative process suggests that bimetallic  $[\text{Ru-Co}]$  species react with one  $\text{Ru}^1(\text{CO})_2$ ,  $\text{Co}(\text{CO})_4^-$ , and  $\text{H}^+$  under a  $\text{CO}/\text{H}_2$  or CO atmosphere under heating, giving unstable, neutral  $[\text{HRuCo}_3(\text{CO})_9(\mu_3\text{-CO})_3]$  with face-bridging CO ligands, which then thermally convert to its isomer  $[\text{HRuCo}_3(\text{CO})_9(\mu_2\text{-CO})_3]$  with edge-bridging CO ligands (Figure 4).

**2.1.4. Anchoring Site of Ruthenium Carbonyl Clusters in Zeolite Cages.** One of the main issues complicating the synthesis and characterization of metal clusters in zeolite is the possible simultaneous formation of metal clusters or crystallites on the exterior zeolite. However, the results of the work here suggest that virtually all the  $[\text{Ru}/\text{Co}_3]$  carbonyl clusters are





**TABLE 6: Catalytic Selectivity on the Intrazeolitic Ru–Co Cluster Catalysts in CO Hydrogenation at Various Temperatures and CO/H<sub>2</sub> Ratios<sup>a</sup>**

catalyst	temp/K	CO conversion (%) CO/H <sub>2</sub>		selectivity (%)									
				hydrocarbons <sup>b</sup> CO/H <sub>2</sub>		oxygenates <sup>b</sup> CO/H <sub>2</sub>		alcohols <sup>b</sup> CO/H <sub>2</sub>		C <sub>2+</sub> alcohols <sup>c</sup> CO/H <sub>2</sub>		aldehydes <sup>c</sup> CO/H <sub>2</sub>	
		1:2	1:1	1:2	1:1	1:2	1:1	1:2	1:1	1:2	1:1	1:2	1:1
[Ru <sub>3</sub> Co] <sub>red</sub> /NaY	498	0.5	0.2	58.4	42.9	41.6	57.1	38.1	46.3	59.0	61.0	3.6	10.3
	523	0.8	0.23	73.4	52.4	36.6	47.6	23.0	40.1	68.0	43.3	3.4	8.7
	548	2.8	0.7	89.8	85.2	10.2	14.8	7.5	10.5	76.0	74.0	2.6	4.1
	573	5.5	1.4	91.8	86.7	8.2	13.3	6.4	11.0	73.2	79.0	1.7	2.9
[RuCo <sub>3</sub> ] <sub>red</sub> /NaY	498	0.4	0.6	39.8	35.7	60.2	64.3	60.2	53.5	49.2	85.6		10.8
	523	2.9	1.2	40.1	58.8	59.9	41.2	58.6	33.5	54.0	90.4	1.3	7.8
	548	6.7	4.5	51.2	74.9	48.8	25.1	43.3	21.4	57.0	84.0	5.5	3.7
	573	15.6	16.6	80.5	81.3	19.5	18.7	16.6	14.3	60.0	82.0	2.9	4.4

<sup>a</sup> CO/H<sub>2</sub> = 0.5; 498–573 K; GHSV = 4800 L (STP) (kg catalyst)<sup>−1</sup> h<sup>−1</sup>; total pressure = 5 bar. <sup>b</sup> Molar ratio of  $\sum_i C_i$  ( $i = 1-6$ , hydrogenates) or ( $i = 1-6$ , oxygenates) or  $i$  ( $i = 1-6$ , alcohols)/ $[\sum_i C_i$  ( $i = 1-6$ , oxygenates) +  $\sum_i C_i$  ( $i = 1-6$ , hydrogenates)]. <sup>c</sup> Molar ratio of  $\sum_i C_i$  ( $i = 2-6$ , alcohols) or  $i$  ( $i = 2-3$ , aldehydes)/ $\sum_i C_i$  ( $i = 1-6$ , oxygenates).

inside zeolite cages. The activity and selectivity of products over the zeolite NaY supported Co or Ru cluster catalysts show a large difference, depending on the cluster size. For Co cluster series catalysts, the [Co<sub>4</sub>]<sub>red</sub>/NaY exhibits a low CO conversion (0.4%) but a high oxygenates selectivity (22.4%) including mainly methanol (8.4%) and 13% C<sub>2+</sub> alcohols and trace aldehydes. The [Co<sub>6</sub>]<sub>red</sub>/NaY shows an improved CO conversion (0.81%) and high yield of light hydrocarbons but a greatly suppressed oxygenates selectivity (16.0%). For Ru cluster series catalysts, the [Ru<sub>3</sub>]<sub>red</sub>/NaY shows activity for hydrocarbon products mainly consisting of methane and 11% oxygenates selectivity (mainly light alcohols), and the [Ru<sub>6</sub>]<sub>red</sub>/NaY produced preferentially methane and heavy hydrocarbons such as C<sub>2</sub>–C<sub>6</sub> but a poor oxygenates selectivity (8.8%).

[Co<sub>4</sub>]<sub>red</sub>/NaY and the [Ru<sub>3</sub>]<sub>red</sub>/NaY show a higher oxygenates selectivity than [Co<sub>6</sub>]<sub>red</sub>/NaY and [Ru<sub>6</sub>]<sub>red</sub>/NaY, whereas [Co<sub>6</sub>]<sub>red</sub>/NaY and [Ru<sub>6</sub>]<sub>red</sub>/NaY exhibit a higher CO conversion than [Co<sub>4</sub>]<sub>red</sub>/NaY and [Ru<sub>3</sub>]<sub>red</sub>/NaY (Table 5). These results suggest that the catalytic properties of the intrazeolitic Co or Ru clusters are size-dependent for CO hydrogenation and are consistent with the observation of the unique reactivity of size-selected gas-phase metallic clusters. The results also suggest that it may be fruitful to search for some reaction for which the zeolite metallic clusters have catalytic properties superior to those of conventionally supported metal catalysts.

For the Ru–Co bimetallic cluster series catalysts, [Ru<sub>3</sub>Co]<sub>red</sub>/NaY shows 2.8% CO conversion and 36.6% oxygenates selectivity, while [RuCo<sub>3</sub>]<sub>red</sub>/NaY exhibits 6.7% CO conversion and 48.8% oxygenates selectivity. Here, it is interesting to note that the Ru–Co bimetallic cluster catalysts exhibit much higher activity and selectivity than the monometallic Ru or Co cluster catalysts. For example, the CO conversion TOF and oxygenates selectivity on bimetallic clusters substantially increased from those on monometallic cluster catalysts (Table 5). Moreover, notably with increasing Co/Ru atomic ratio in Ru–Co bimetallic clusters, the activity and oxygenates selectivity highly increased (Table 5). The aforementioned EXAFS data proved the interaction of Ru and Co in [RuCo<sub>3</sub>]<sub>red</sub>/NaY catalyst. These interaction sites could act as the active species and have a strong synergy effect in enhancing CO conversion and catalytic oxygenate formation.

**2.2.2 Effects of Heat Transfer and CO/H<sub>2</sub> Ratio in Bimetallic Ru–Co Cluster Catalytic CO Hydrogenation.** Table 6 presents the temperature dependence for CO hydrogenation on [Ru<sub>3</sub>Co]<sub>red</sub>/NaY and [RuCo<sub>3</sub>]<sub>red</sub>/NaY catalysts. An obvious feature is that oxygenates selectivity decreases, and that CO conversion, hydrocarbons selectivity, and C<sub>2+</sub> oxygenates

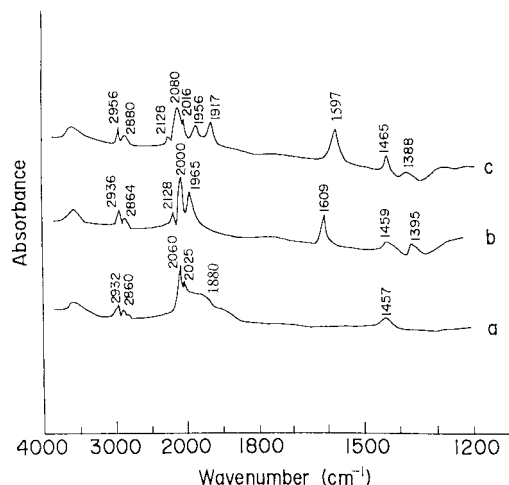


**Figure 6.** Infrared spectra characterizing the reacted catalysts under a mixed CO and H<sub>2</sub> (CO/H<sub>2</sub> = 0.5) atmosphere at 463 K for 5 h: (a) [Ru<sub>3</sub>]<sub>red</sub>/Na<sub>56</sub>Y; (b) [Ru<sub>3</sub>Co]<sub>red</sub>/Na<sub>56</sub>Y; (c) [RuCo<sub>3</sub>]<sub>red</sub>/Na<sub>56</sub>Y.

selectivity increase, with increasing temperature. The products distribution shows that C<sub>2</sub> alcohols are predominant in the oxygenates at higher temperatures.

Whether [Ru<sub>3</sub>Co]<sub>red</sub>/NaY or [RuCo<sub>3</sub>]<sub>red</sub>/NaY catalyst, the use of CO-rich syngas (CO/H<sub>2</sub> = 1) in CO hydrogenation resulted in a considerable decrease in CO conversion and an increase in C<sub>2+</sub> alcohols selectivity. When the CO/H<sub>2</sub> ratio was varied from 0.5 to 1.0 on the [Ru<sub>3</sub>Co]<sub>red</sub>/NaY at 548 K, CO conversion reduced rapidly from 2.8% to 0.7%, and oxygenates selectivity greatly increased from 10.2% to 14.8% (Table 6). These observations provide some evidence that increasing the CO/H<sub>2</sub> ratio in syngas, the Co/Ru atomic ratio in Ru–Co bimetallic catalysts, and the heat transfer promoted higher alcohols yields.

**2.2.3 Infrared Spectroscopic Studies for CO Hydrogenation on the Cluster Catalysts.** Infrared spectra characterizing the cluster catalysts under syngas were investigated. Syngas (CO/H<sub>2</sub> = 0.5) was passed through the infrared sample wafer at a flow rate of 20 mL/min for 5 h at 463 K. After evacuation for 10 min at 298 K to remove physical or weakly chemisorbed CO and H<sub>2</sub>, the infrared spectrum of the [Ru<sub>3</sub>]<sub>red</sub>/NaY catalyst shows broad bands at 2060, 2025, 1880, and 1457 cm<sup>−1</sup> and two weak bands at 2932, 2860 cm<sup>−1</sup> (Figure 6a). The broad bands at 2060–1880 cm<sup>−1</sup> are assigned to the terminal CO on the Ru cluster surface,<sup>32,33</sup> and weak bands at 2932 and 2860 cm<sup>−1</sup> are due to the C–H stretching vibration, while the 1457 cm<sup>−1</sup> band is ascribed to the C–H deformation vibration.<sup>34</sup> On the other hand, the bimetallic [Ru<sub>3</sub>Co]<sub>red</sub>/NaY catalyst shows new



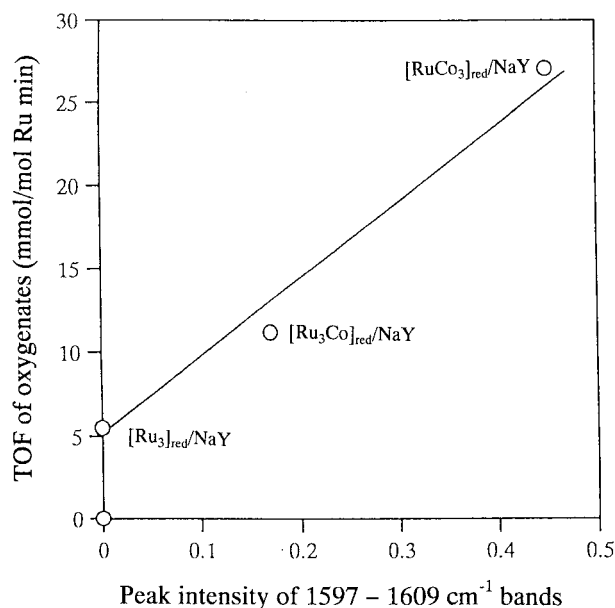


**Figure 7.** Rate of oxygenates formation in CO hydrogenation versus the 1597–1609  $\text{cm}^{-1}$  band intensity on  $[\text{Ru}_3]_{\text{red}}/\text{NaY}$ ,  $[\text{Ru}_3\text{Co}]_{\text{red}}/\text{Na}_5\text{Y}$ , and  $[\text{RuCo}_3]_{\text{red}}/\text{Na}_5\text{Y}$  catalysts.

bands at 1609 and 1395  $\text{cm}^{-1}$  (Figure 6b), and the bimetallic  $[\text{RuCo}_3]_{\text{red}}/\text{NaY}$  catalyst exhibits new bands at 1597, 1388  $\text{cm}^{-1}$  (Figure 6c), in addition to the bands that appeared in the  $[\text{Ru}_3]_{\text{red}}/\text{NaY}$  catalyst. By comparison of the intensity of these bands with the rate of oxygenates formation on the catalysts, a good linear relationship is observed between the 1597–1609  $\text{cm}^{-1}$  band intensity and the rate of oxygenate formation (Figure 7). However, there was no correlation between the 2080–1880  $\text{cm}^{-1}$  band intensities and the rate of oxygenate formation. These results suggest that the adspecies band at 1597–1609  $\text{cm}^{-1}$  plays an important role in the production of oxygenates. This adspecies may be an intermediate of oxygenate formation from CO hydrogenation.

In addition, the 1597–1609  $\text{cm}^{-1}$  band intensity varies with  $\text{CO}/\text{H}_2$  ratio. The plot of the 1609  $\text{cm}^{-1}$  band intensity and oxygenates selectivity over the  $[\text{RuCo}_3]_{\text{red}}/\text{NaY}$  catalyst versus the  $\text{CO}/\text{H}_2$  ratio indicated that the oxygenates selectivity and 1609  $\text{cm}^{-1}$  band intensity linearly increases with increasing  $\text{CO}/\text{H}_2$  ratio (Figure 8).

**2.2.4 Assignment of Infrared Bands in CO Hydrogenation.** To confirm the assignment of the adspecies under CO hydrogenation,  $^{13}\text{C}$ - and  $\text{D}$ -labeled CO and  $\text{H}_2$  were used. As shown in Figure 9, the reaction of  $^{13}\text{CO} + \text{H}_2$  on the  $[\text{RuCo}_3]_{\text{red}}/\text{NaY}$ , the bands shift from 1597 to 1555  $\text{cm}^{-1}$  and from 1388 to 1356  $\text{cm}^{-1}$  (Figure 9b) because of isotopic effects, suggesting that the 1597 and 1388  $\text{cm}^{-1}$  bands in Figure 9a or in Figure 6c are closely related to the infrared bands of CO groups.

The infrared spectrum of  $\text{D}_2 + \text{CO}$  on the  $[\text{RuCo}_3]_{\text{red}}/\text{NaY}$  shows a variation in bands at 2846, 2768, 2021, 1976, 1588, and 1388  $\text{cm}^{-1}$  (Figure 9c) from that shown in Figure 9a. The 1588  $\text{cm}^{-1}$  is reasonably assigned to only a 9  $\text{cm}^{-1}$  shift from the 1597  $\text{cm}^{-1}$  band, while the 2846 and 2768  $\text{cm}^{-1}$  bands appear at a 110–112  $\text{cm}^{-1}$  shift from the 2956 and 2880  $\text{cm}^{-1}$  bands. The former suggests that the 1597  $\text{cm}^{-1}$  band could not be assigned to the  $\nu_{\text{C-H}}$  deformation vibration, while the latter is indicative of the adspecies containing a C–H bond. This is in line with the C–D stretch/deformation vibration band causing a large shift from the C–H stretch/deformation vibration band.<sup>35</sup>

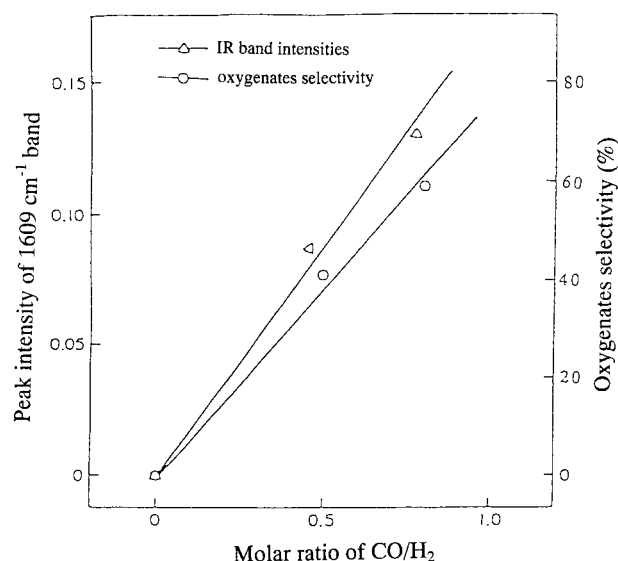


**Figure 8.** Plot of the 1597  $\text{cm}^{-1}$  band intensity and the oxygenates selectivity versus the  $\text{CO}/\text{H}_2$  molar ratio for CO hydrogenation over the  $[\text{Ru}_3\text{Co}]_{\text{red}}/\text{Na}_5\text{Y}$  catalyst.

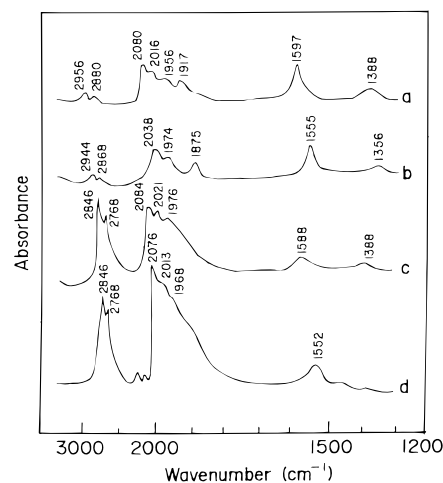


**Figure 9.** Infrared spectra characterizing  $[\text{RuCo}_3]_{\text{red}}/\text{NaY}$  under (a)  $\text{CO} + \text{H}_2$ , (b)  $^{13}\text{CO} + \text{H}_2$ , (c)  $\text{CO} + \text{D}_2$ , (d)  $^{13}\text{CO} + \text{D}_2$  atmosphere at 0.5 of  $\text{CO}/\text{H}_2$  at 463 K.

With the exposure of the  $[\text{RuCo}_3]_{\text{red}}/\text{NaY}$  to the  $^{13}\text{CO} + \text{D}_2$  atmosphere, the 1597  $\text{cm}^{-1}$  band shifts to 1552  $\text{cm}^{-1}$  and the 2956–2880  $\text{cm}^{-1}$  bands shift to 2846–2768  $\text{cm}^{-1}$  (Figure 9d). These shifts, due to the isotopic effect of both  $^{13}\text{CO}$  and  $\text{D}_2$ , respectively, are consistent with the further inference that the adspecies contains both C–H and C–O bonds.

On the basis of these isotopic studies of the adspecies, two possible structures, such as the formate and formyl species, are suggested. Solymosi et al. observed the infrared adsorption bands of formic acid on  $\text{Rh}/\text{Al}_2\text{O}_3$ <sup>36</sup> and  $\text{Ru}/\text{Al}_2\text{O}_3$ <sup>37</sup> located at 1585, 1392, and 1375  $\text{cm}^{-1}$  under  $\text{CO} + \text{H}_2$  reaction. These bands shifted under  $\text{CO} + \text{D}_2$  to 1583, 1350, and 1345  $\text{cm}^{-1}$ , respectively. The 1585 and 1375  $\text{cm}^{-1}$  bands were attributed to the asymmetric and symmetric OCO stretching vibration of the formate species, and the 1392  $\text{cm}^{-1}$  band was assigned to the deformation mode of surface formate. The present adspecies could not be simply assigned to a formate, since our isotopic experimental results are not in line with the work of Solymosi et al.<sup>36,37</sup> Notably, if the formyl species was a model of the adspecies, it is very interesting to note that the theoretical results<sup>35</sup> are identical to our isotopic experimental results. Therefore, the 1597  $\text{cm}^{-1}$  band is assigned to the CO stretching

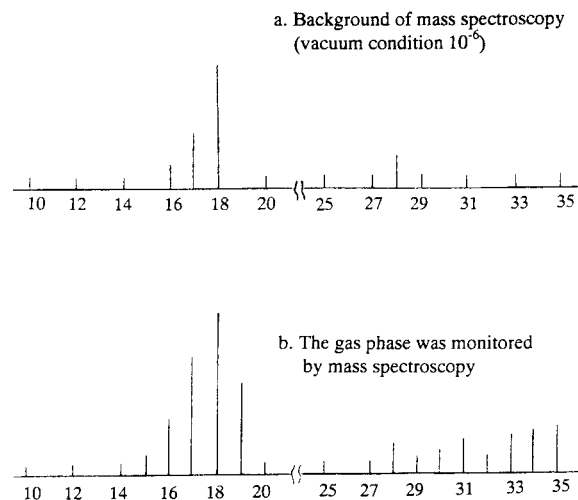


**Figure 10.** Mass analysis for the  $D_2$  reaction with adspecies resulting from CO hydrogenation.

frequency of a surface formyl, and the  $2956\text{--}2880\text{ cm}^{-1}$  bands are ascribed to the CH stretching frequency in this surface formyl species. Some analogous infrared bands due to a formyl coordinated model have been reported in  $Os(CHO)(H)(CO_2)(PPh_3)$  ( $\nu_{CO} = 1601\text{ cm}^{-1}$ ) and  $Re(Et)(CO)(NO)(CHO)$  ( $\nu_{CO} = 1624\text{ cm}^{-1}$ ),<sup>38</sup> which further confirms that the assignment of  $1597\text{ cm}^{-1}$  is consistent with the CO stretching band of surface formyl adspecies ( $:HC=O$ ). When 100 Torr of  $D_2$  reacted with the adspecies, the mass analysis of the produced gas shows two regions with mass numbers at 15–19 and 30–35, which are assigned to  $CHD_3$  and  $CHD_2OD$  or  $CD_3OH$ , respectively (Figure 10). This provides an informative picture that the adspecies consists of one H and one CO group. Generally, the  $\nu_{CO}$  of the formyl species should appear near  $1700\text{ cm}^{-1}$ . Here,  $1597\text{ cm}^{-1}$  exhibits a  $100\text{ cm}^{-1}$  red shift, suggesting the decrease of the C–O bond and/or the increase of the C–O antibond. As mentioned in section 2.1.3, the decarbonylated  $[RuCo_3]_{red}/NaY$  contains Ru–Co interaction sites. Since the Co radius is smaller than the Ru radius,  $1\pi$  electrons at the O end of CO tend to transfer to Co, whereas Ru donates electrons into the  $2\pi$  orbital of CO, forming  $2\pi^*$  antibond. When the formyl species is adsorbed on the adjacent Ru–Co sites, we therefore propose that the oxygen end of the formyl species interacts with Co and that the C end of the formyl species interacts with the Ru of adjacent Ru–Co sites, as shown in the model in Figure 11a. These reactions would reduce the C–O bond strength and strengthen the C–O antibond strength, accompanied by a red shift of  $\nu_{CO}$  in the formyl adspecies. This is similar to a previous suggestion that bifunctional chemisorption of CO occurring on conventional Rh–Mn, Rh–Ti, and Rh–Zr/SiO<sub>2</sub> catalysts induced a large reduction of CO frequency.<sup>15,16</sup>

It is interesting to note from the infrared spectra that the  $1597\text{ cm}^{-1}$  band intensity decreases and that a new band at  $1568\text{ cm}^{-1}$  develops gradually under CO hydrogenation at  $463\text{--}498\text{ K}$  (Figure 12a). The infrared spectrum of  $[RuCo_3]_{red}/NaY$  after 5 h of reaction at  $513\text{ K}$  provides a  $1575\text{ cm}^{-1}$  band, which may arise from the overlapping of  $1568$  and  $1597\text{ cm}^{-1}$  bands (Figure 12b). The  $1575\text{ cm}^{-1}$  band grows in intensity with increasing temperature, and a  $1568\text{ cm}^{-1}$  shoulder band becomes larger (parts b–d of Figure 12). This suggests that the surface formyl adspecies underwent a combination with  $C_nH_{2n}$  adspecies or  $CH_2$  adspecies, forming new  $C_nH_{2n+1}CO$  or  $CH_3CO$  adspecies on the adjacent Ru–Co sites (parts c and d of Figure 11) with a characteristic CO stretch frequency at  $1568\text{ cm}^{-1}$ . In addition, the C–H stretch at  $2960$  and  $2880\text{ cm}^{-1}$  further confirmed the

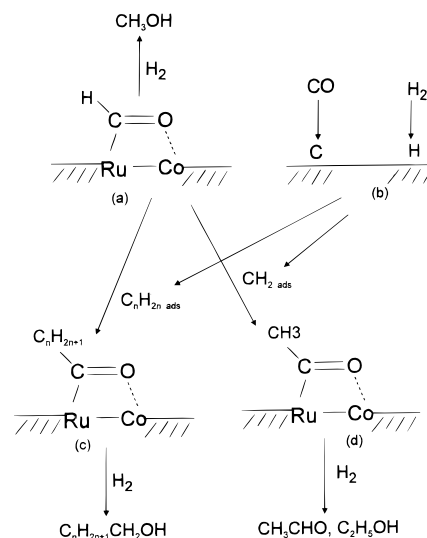


**Figure 11.** Proposed mechanism for oxygenates formation from CO hydrogenation on Ru–Co adjacent sites of  $[RuCo_3]_{red}/NaY$  catalyst.

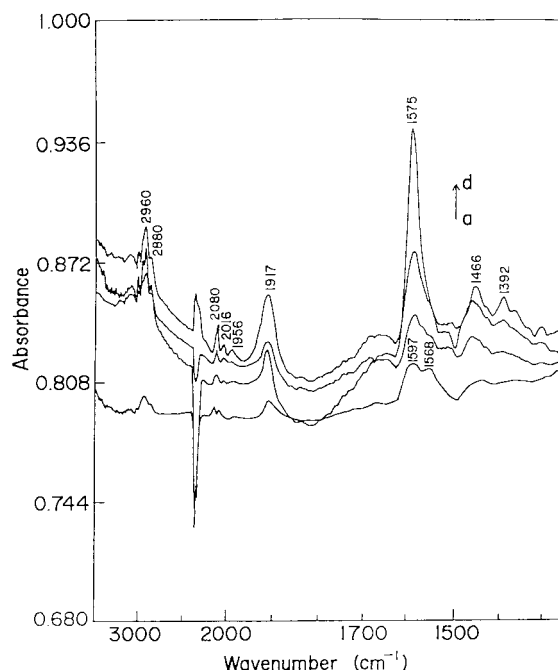


**Figure 12.** Infrared spectra characterizing  $[RuCo_3]_{red}/NaY$  in CO hydrogenation with increasing temperature.

growing  $C_nH_{2n+1}CO$  or  $CH_3CO$  adspecies. This is associated with the increase of high  $C_{2+}$  alcohols on bimetallic Ru–Co cluster catalysts at temperatures above  $473\text{ K}$  (Table 6). Thus, it is conceivable that the promotion of oxygenates formation could be explained in terms of the two-site activation of HCO with an Ru–Co cluster to enhance the migratory HCO insertion into  $CH_2$  or  $CH_nH_{2n}$  adspecies, enhancing the successive hydrogenation to an alcohol (parts c and d of Figure 11).

In contrast, the  $1597\text{ cm}^{-1}$  adspecies cannot be formed on monometallic Ru or Co cluster catalysts under CO hydrogenation at  $463\text{ K}$ . This is in agreement with the literature<sup>39</sup> in that formyl species ( $H_2CO$ ) adsorbed on transition metals are unstable and easily convert into carbonyl hydride species  $H_xM-CO$  ( $x = 1, 2$ ). Thus, we suggest that the lack of the formyl adspecies is the reason for poor oxygenates selectivity on monometallic Ru or Co cluster catalysts.

On the basis of reaction kinetics, infrared spectroscopy, and EXAFS studies for characterization of the Ru–Co interaction

**TABLE 7: Kinetics Parameters for Deactivation and Regeneration of [Co<sub>6</sub>]<sub>red</sub>/NaY, [Ru<sub>3</sub>Co]<sub>red</sub>/NaY, and [RuCo<sub>3</sub>]<sub>red</sub>/NaY Catalysts<sup>a</sup>**

catalyst	CO conversion (%)	selectivity (%)				
		hydrocarbons <sup>b</sup>	oxygenates <sup>b</sup>	alcohols <sup>b</sup>	C <sub>2</sub> + alcohols <sup>c</sup>	aldehydes <sup>c</sup>
[Co <sub>6</sub> ] <sub>red</sub> /NaY						
20 h after initial startup	0.10	12.7	87.3	87.3	35.4	
100 h after initial startup	0.03	20.5	79.5	79.5	21.2	
after H <sub>2</sub> treatment <sup>d</sup>	0.035	34.1	65.9	65.9	17.8	
[Ru <sub>3</sub> Co] <sub>red</sub> /NaY						
20 h after initial startup	0.5	58.4	41.6	38.1	59.0	3.6
100 h after initial startup	0.37	64.9	35.1	32.8	49.8	2.2
after H <sub>2</sub> treatment <sup>d</sup>	0.49	57.3	42.7	38.7	64.9	3.4
[RuCo <sub>3</sub> ] <sub>red</sub> /NaY						
20 h after initial startup	0.6	35.7	64.3	53.5	85.6	10.8
100 h after initial startup	0.46	47.3	52.7	41.9	44.6	6.5
after H <sub>2</sub> treatment <sup>d</sup>	0.58	38.3	61.7	54.7	80.2	10.7

<sup>a</sup> CO/H<sub>2</sub> = 0.5 for [Co<sub>6</sub>]<sub>red</sub>/NaY and [Ru<sub>3</sub>Co]<sub>red</sub>/NaY; CO/H<sub>2</sub> = 1 for [RuCo<sub>3</sub>]<sub>red</sub>/NaY; 498 K; GHSV = 4800 L (STP) (kg catalyst)<sup>-1</sup> h<sup>-1</sup>; total pressure = 5 bar. <sup>b</sup> Molar ratio of Σ<sub>i</sub>C<sub>i</sub> (*i* = 1–6, hydrogenates) or (*i* = 1–6, oxygenates) or *i* (*i* = 1–6, alcohols)/Σ<sub>i</sub>C<sub>i</sub> (*i* = 1–6, oxygenates) + Σ<sub>i</sub>C<sub>i</sub> (*i* = 1–6, hydrogenates). <sup>c</sup> Molar ratio of Σ<sub>i</sub>C<sub>i</sub> (*i* = 2–6, alcohols) or *i* (*i* = 2–3, aldehydes)/Σ<sub>i</sub>C<sub>i</sub> (*i* = 1–6, oxygenates). <sup>d</sup> H<sub>2</sub> regeneration treatment at 473 K for 4–6 h.

sites for [RuCo<sub>3</sub>]<sub>red</sub>/NaY, we speculate that Co may play a role not only in anchoring Ru atoms without their aggregation but also in affecting catalytic performance to promote oxygenate formation. The effect may be ascribed to Co interaction with the O end of the formyl adspecies and electron transfer from cobalt to ruthenium. Cobalt, with an abundant electron density that results from 1 $\pi$  electrons of the formyl adspecies, will tend to donate electrons to ruthenium to fill some of its d levels. This possibly produces effective electron configurations of ruthenium that are closer to the electronic configurations of elements to its right in the periodic table, i.e., to rhodium or palladium (rhodium or palladium has larger reactivity with CO than ruthenium).<sup>40</sup> Such an electron transfer or cobalt-bonding Ru–formyl species is in accordance with expectations of further electron donation into 2 $\pi^*$  CHO orbitals,<sup>40</sup> causing a decrease in  $\nu_{\text{CO}}$  of the formyl adspecies. The adjacent Ru–Co sites of the [RuCo<sub>3</sub>]<sub>red</sub>/NaY are thus suggested to have a large effect in suppressing dissociation of the formyl species and in promoting formyl species mobility on the cluster surface, thereby favoring oxygenate formation.

**2.2.5. Deactivation and Regeneration of the Cluster Catalysts.** An activity profile of [Co<sub>6</sub>]<sub>red</sub>/NaY, [Ru<sub>3</sub>Co]<sub>red</sub>/NaY, and [RuCo<sub>3</sub>]<sub>red</sub>/NaY is shown in Table 7. Monometallic or bimetallic cluster catalysts showed stable activity in a period of 3–20 h.

Extended testing of the catalysts in syngas (CO/H<sub>2</sub> = 1 or 0.5) led to deactivation. After 25 h, the [Co<sub>6</sub>]<sub>red</sub>/NaY deactivates, as evidenced by a decrease of the CO conversion, while the rate of oxygenates formation slowly decreases in the order C<sub>5</sub> > C<sub>4</sub> > C<sub>3</sub> > C<sub>2</sub> > C<sub>1</sub> alcohols. This deactivation is ascribed to carbon deposits on the cluster surface. The deactivation of the bimetallic [Ru<sub>3</sub>Co]<sub>red</sub>/NaY and [RuCo<sub>3</sub>]<sub>red</sub>/NaY is much slower than that over the [Co<sub>6</sub>]<sub>red</sub>/NaY catalyst. This is consistent with the suggestion that the retarding effect of Ru–Co sites in the carbon deposition reaction influences deactivation.

A hydrogen treatment under reaction conditions (473 K, 4–6 h) did not restore the initial reaction rates and selectivities on the monometallic [Co<sub>6</sub>]<sub>red</sub>/NaY catalyst. On both the [Ru<sub>3</sub>Co]<sub>red</sub>/NaY and the [RuCo<sub>3</sub>]<sub>red</sub>/NaY catalysts, however, this treatment restored the rates and selectivities to values similar to those observed during the initial 3–20 h (Table 7). This suggests an active site regeneration by hydrogenation and hydrogenolysis of residual carbonaceous deposits on the Ru–Co cluster sur-

face. On the other hand, the deactivation and no regeneration of the [Co<sub>6</sub>]<sub>red</sub>/NaY catalyst suggest that Co particles are growing, or poisoning the active sites by the deposition of unreactive graphitic carbon from syngas.

### 3. Experimental Section

**3.1. Sample Preparation.** The synthesis of [Co<sub>4</sub>(CO)<sub>12</sub>]/NaY, [Co<sub>6</sub>(CO)<sub>16</sub>]/NaY, [Ru<sub>3</sub>(CO)<sub>12</sub>]/NaY, [Ru<sub>6</sub>(CO)<sub>18</sub>]<sup>2-</sup>/NaY, and [HRu<sub>3</sub>Co(CO)<sub>13</sub>]/NaY were described elsewhere.<sup>4–9</sup> Here, we report the synthesis of zeolite-encapsulated [RuCo<sub>3</sub>(CO)<sub>12</sub>]. The NaY zeolite-supported Ru sample (3.2 wt % loading or 6 Ru per unit cell) was prepared by the cation-exchange of NaY zeolite (HSZ-320NAA, lot no. D1-9915, Si/Al = 2.8, surface area of 910 m<sup>2</sup> g<sup>-1</sup>) with Ru(NH<sub>3</sub>)<sub>6</sub>Cl<sub>3</sub> (Strem Chemical Co.) solution at 300 K for 2 days followed by filtration, washing with deionized water, and drying at 393 K. The ion-exchanged Ru(NH<sub>3</sub>)<sub>6</sub>/NaY was red-colored (UV–vis spectrum,  $\lambda_{\text{max}}$  = 555 nm). After it was exposed to a CO/H<sub>2</sub> atmosphere (200 Torr/200 Torr) in a closed circulating reactor with temperature-programmed heating from 300 to 413 K, a yellow sample was obtained (UV–vis spectrum,  $\lambda_{\text{max}}$  = 235, 285 nm). The infrared spectrum of the yellow sample showed  $\nu_{\text{CO}}$  bands at 2054 (vs) and 1937 (s) cm<sup>-1</sup> due to [HRu<sub>6</sub>(CO)<sub>18</sub>]<sup>1-</sup>/NaY (one [HRu<sub>6</sub>(CO)<sub>18</sub>]<sup>1-</sup> per unit cell).<sup>8</sup> The [HRu<sub>6</sub>(CO)<sub>18</sub>]<sup>1-</sup>/NaY was subsequently exposed to 400 Torr of O<sub>2</sub> from 298 to 473 K and held at 473 K for 2 h to give decarbonylated Ru clusters, [Ru<sub>x</sub>]<sub>ox</sub>/NaY.<sup>8</sup>

The Co<sub>2</sub>(CO)<sub>8</sub> was dissolved in dry deoxygenated tetrahydrofuran (THF), and the [Ru<sub>x</sub>]<sub>ox</sub>/NaY pellet was then immersed in a THF of Co<sub>2</sub>(CO)<sub>8</sub> (Co/Ru = 2.7–3.2 atomic ratio) until the brown color of the THF Co<sub>2</sub>(CO)<sub>8</sub> solution disappeared. The pellet was then exposed to a CO/H<sub>2</sub> mixture (CO/H<sub>2</sub> = 300 Torr/150 Torr) in an infrared cell and subsequently heated from 298 to 353 K.

The concentrations of Ru and Co in the samples were determined using an inductively coupled plasma atomic emission (ICP) spectrometer. Attempts to extract organometallic species from the NaY-supported sample were carried out with THF solution.

**3.2. Characterization of Samples. Infrared Spectroscopy.** In situ infrared spectra of the samples were recorded with a Shimadzu FT-IR 4200 spectrometer with 20–100 coadded scans at 2 cm<sup>-1</sup> resolution. The samples were pressed into a self-supporting wafer (8 mg cm<sup>-2</sup>) in an N<sub>2</sub>-atmosphere box and



mounted in a quartz infrared cell with CaF<sub>2</sub> windows that was connected to a Pyrex-glass line vacuum (10<sup>-5</sup> Torr) with closed circulation. The infrared cell was equipped with an electric heater and a liquid N<sub>2</sub> reservoir for high- and low-temperature measurements. The contribution of the gas was compensated by using a reference infrared cell having the same optical length as the sample cell. Before use, all gases were passed through traps to remove water and/or oxygen.

**EXAFS Spectroscopy.** EXAFS measurements were carried out at the Photon Factory in Japan National Laboratory for High Energy Physics (KEF-PF) using synchrotron radiation with an electron energy of 2.5 GeV at currents of 150–350 mA. The amount of sample in a wafer was calculated at the Co or Ru K absorption edge, and the sample wafers were stored in specially designed Pyrex-glass cells with Kapton film windows (50 nm thick). The spectra at the Co K-edge and the Ru K-edge were measured at 296 K under vacuum using a Si (111) double-crystal monochromator.

**EXAFS Data Analysis.** The EXAFS data were extracted from the measured absorption spectra by standard methods.<sup>41,42</sup> The normalization was done by dividing the absorption intensities by the height of the absorption edge and subtracting the background using cubic-spline routines. The final EXAFS function was obtained by averaging the individual background-subtracted and normalized EXAFS data (two scans for each sample). The main contributions to the spectra were isolated by inverse Fourier transformation of the final EXAFS function over a selected range in *R* space. The analysis was performed on these Fourier filtered data. The parameters characterizing high-*Z* (Co, Ru and O) and low-*Z* (C) contributions were reliably determined by multiple-shell fitting in *k* space (*k* is the wave vector) and *R* space (*R* is the distance from the absorbing atom) with application of *K*<sup>3</sup> weighting of the Fourier transform. The accuracy of parameters was estimated as 0.02 <  $\sigma$  < 0.08 and -10 <  $\Delta E_0$  < 10. The residual factor

$$\frac{\int |k^3 \chi^{\text{obs}}(k) - k^3 \chi^{\text{calc}}(k)|^2 dk}{|k^3 \chi^{\text{obs}}(k)|^2 dk}$$

was less than 15% for optimized coordination numbers and bond lengths.<sup>42</sup>

**3.3. Catalytic Measurement for CO Hydrogenation.** The CO hydrogenation reaction was carried out at 473–573 K in a continuous flow stainless steel reactor (inner diameter of 14 mm and 240 mm long tubing), where 1.0 g of the catalyst was charged. A mixture of CO and H<sub>2</sub> (CO/H<sub>2</sub> = 0.5–1.0 molar ratio, 5.0 × 10<sup>5</sup> Pa) was introduced into the reactor. The gas hourly space velocity (GHSV) employed was 4800 L (STP) (kg catalyst)<sup>-1</sup> h<sup>-1</sup>. All experimental data were obtained under steady-state conditions that were usually maintained for 20–25 h before changing the reaction conditions to obtain another set of data. The long-term performance of each catalyst was determined in the reaction run up to 100 h.

Oxygenated products such as CH<sub>3</sub>OH, CH<sub>3</sub>CHO, and C<sub>2</sub>H<sub>5</sub>OH were collected in a water trap (50 mL of H<sub>2</sub>O) by bubbling the effluent gas through it and were analyzed by a Shimadzu GC-8APF gas chromatograph with a flame ionization detector using a 4 mm i.d. × 2 m Chromosorb 101 (60–80 mesh) column with a heating-program for 35–160 °C and acetone as an internal standard. CO, CO<sub>2</sub>, and hydrocarbons were separated by using a Shimadzu GC-8AIF gas chromatograph with a thermal conductivity detector using a 4 mm i.d. × 2 m Unibeads-1s (80–100 mesh) column at 70 °C. For each gas

chromatograph, concentrations of the products were calculated with an integrator (Shimadzu Chromatopac CR-3A).

## References and Notes

- (1) Preuss, E.; Linden, G.; Peuckert, M. *J. Phys. Chem.* **1985**, *89*, 2955.
- (2) Mortier, W. J.; Schoonheydt, R. A. *Prog. Solid State Chem.* **1985**, *16*, 1.
- (3) Barthomeuf, D. In *Zeolite: Science and Technology*; NATO ASI Series, Series E: Applied Sciences 80; Martinus Nijhoff: The Hague, 1984; p 137.
- (4) Shen, G. C.; Ichikawa, M. *J. Chem. Soc., Faraday Trans.* **1997**, *93*, 1185.
- (5) Shen, G. C.; Shido, T.; Ichikawa, M. *J. Phys. Chem.* **1996**, *100*, 16947.
- (6) Shen, G. C.; Ichikawa, M. *J. Phys. Chem.* **1996**, *100*, 14265.
- (7) Shen, G. C.; Liu, A. M.; Tanaka, T.; Ichikawa, M. Manuscript in preparation.
- (8) Shen, G. C.; Liu, A.-M.; Shido, T.; Ichikawa, M. *Top. Catal.* **1995**, *2*, 141.
- (9) Shen, G. C.; Liu, A. M.; Ichikawa, M. *J. Chem. Soc., Faraday Trans.* **1998**, *94*, 1532.
- (10) Ichikawa, M.; Rao, L.-F.; Ito, T.; Fukuoka, A. *Faraday Discuss., Chem. Soc.* **1989**, *87*, 232.
- (11) Muettetries, L.; Rhodin, T. N.; Band, E.; Bruker, C. F.; Prezer, W. R. *Chem. Rev.* **1979**, *79*, 9.
- (12) Yermakov, Y. I.; Kuznetsov, B. N.; Zakharov, V. A., Eds. *Catalysis by Supported Complexes*; Elsevier: Amsterdam, 1981.
- (13) Gates, B. C.; Gucci, L.; Knözinger, H., Eds. *Metal Clusters in Catalysis*; Elsevier: Amsterdam, 1996.
- (14) Ozin, G. A. In *Materials Chemistry*; Interrante, L. V., Casper, L. A., Ellis, A. B., Eds.; American Chemical Society: Washington, DC, 1995; pp 335–371.
- (15) Ichikawa, M.; Fukushima, T.; Yokoyama, T.; Kosugi, N.; Kuroda, H. *J. Phys. Chem.* **1986**, *90*, 1222.
- (16) Niemantsverdriet, J. W.; van der Krann, A. M.; Delgass, W. N. *J. Catal.* **1984**, *89*, 138.
- (17) Niemantsverdriet, J. W.; van Kaam, J. A. C.; Flipes, C. F. J.; van der Krann, A. M. *J. Catal.* **1985**, *96*, 58.
- (18) Ichikawa, M.; Fukushima, T. *J. Phys. Chem.* **1985**, *89*, 1564.
- (19) Johnson, B. F. G.; Lewis, J.; Raithby, P. R.; Suss, G. *J. Chem. Soc., Dalton Trans.* **1976**, 1356.
- (20) Hidai, M.; Orisaku, M.; Ue, M.; Koyasu, Y.; Kodama, T.; Uchida, Y. *Organometallics* **1983**, *2*, 292.
- (21) Teo, B. K. *EXAFS: Basic Principles and Data Analysis*; Springer: Berlin, 1986.
- (22) Lamb, H. H.; Gates, B. C.; Knözinger, H. *Angew. Chem., Int. Ed. Engl.* **1988**, *27*, 1127.
- (23) Rao, L.-F.; Fukuoka, A.; Kosugi, N.; Kuroda, H.; Ichikawa, M. *J. Phys. Chem.* **1990**, *94*, 5317.
- (24) (a) Schneider, R. L.; Howe, R. R.; Watters, K. L. *Inorg. Chem.* **1984**, *23*, 4600. (b) Connaway, M. C.; Hanson, B. E. *Inorg. Chem.* **1986**, *25*, 1445.
- (25) Liu, A. M.; Shido, T.; Ichikawa, M. *J. Chem. Soc., Chem. Commun.*, in press.
- (26) Yokomizo, G. H.; Louis, C.; Bell, A. T. *J. Catal.* **1989**, *120*, 1.
- (27) Breck, D. W. *Zeolite Molecular Sieves*; Wiley: New York, 1974.
- (28) Eulenberger, G. R.; Shoemaker, D. P.; Keil, J. G. *J. Phys. Chem.* **1967**, *71*, 1812.
- (29) Fitch, A. N.; Jobic, H.; Renouprez, A. *J. Phys. Chem.* **1986**, *90*, 1311.
- (30) Jelinek, P. Ph.D. Thesis, Department of Chemistry, University of Toronto, 1993.
- (31) Fukuoka, A.; Kimura, T.; Kosugi, N.; Kuroda, H.; Minai, Y.; Sakai, Y.; Tominaga, T.; Ichikawa, M. *J. Catal.* **1990**, *126*, 434.
- (32) Brown, M. F.; Gonzalez, R. D. *J. Phys. Chem.* **1976**, *80*, 1731.
- (33) Kuznetsov, V. L.; Bell, A. T.; Yermakov, Y. *J. Catal.* **1980**, *65*, 374.
- (34) Luchesi, P. J.; Cater, J. L.; Yates, D. J. C. *J. Phys. Chem.* **1962**, *66*, 1451.
- (35) Pinchas, S.; Laulicht, I. In *Infrared Spectra of Labeled Compounds*; Academic Press: New York, 1971.
- (36) Solymosi, F.; Erdohelyi, A.; Kocsis, M. *J. Catal.* **1980**, *65*, 428.
- (37) Datta Betta, R. A.; Shelef, M. *J. Catal.* **1977**, *48*, 48.
- (38) Brown, K. L.; Clark, G. R.; Headford, C. E. L.; Marsden, K.; Roper, W. R. *J. Am. Chem. Soc.* **1979**, *101*, 505.
- (39) Yates, J. T.; Worley, S. D.; Duncan, T. M.; Vaughan, R. W. *J. Chem. Phys.* **1979**, *70*, 1225.
- (40) Klier, K. *Adv. Catal.* **1982**, *31*, 243–310.
- (41) van Zon, J. B. A. D.; Koningsberger, D. C.; Van't Blik, H. F. J.; Sayers, D. E. *J. Chem. Phys.* **1985**, *12*, 5742.
- (42) Kosugi, N.; Kuroda, H. *Program EXAFS 2*; Research Center for Spectrochemistry, University of Tokyo: Tokyo, 1988.